Epitaxial graphene on ruthenium

PETER W. SUTTER*, JAN-INGO FLEGE AND ELI A. SUTTER
Center for Functional Nanomaterials, Brookhaven National Laboratory, Upton, New York 11973, USA
*e-mail: psutter@bnl.gov

Published online: 6 April 2008; doi:10.1038/nmat2166

Graphene has been used to explore the fascinating electronic properties of ideal two-dimensional carbon, and shows great promise for quantum device architectures. The primary method for isolating graphene, micromechanical cleavage of graphite, is difficult to scale up for applications. Epitaxial growth is an attractive alternative, but achieving large graphene domains with uniform thickness remains a challenge, and substrate bonding may strongly affect the electronic properties of epitaxial graphene layers. Here, we show that epitaxy on Ru(0001) produces arrays of macroscopic single-crystalline graphene domains in a controlled, layer-by-layer fashion. Whereas the first graphene layer indeed interacts strongly with the metal substrate, the second layer is almost completely detached, shows weak electronic coupling to the metal, and hence retains the inherent electronic structure of graphene. Our findings demonstrate a route towards rational graphene synthesis on transition-metal templates for applications in electronics, sensing or catalysis.

Graphene, a two-dimensional honeycomb lattice of sp^2-bonded carbon atoms[1], has shown a wealth of exceptional properties such as anomalous behaviour in the integer quantum Hall effect[2] and in quasiparticle coupling[3], which are signatures of charge carriers behaving as massless Dirac fermions. A very high carrier mobility[4] and long-range ballistic transport at room temperature[5], quantum confinement in nanoscale ribbons[6] and single-molecule gas detection sensitivity[7] qualify graphene as a promising material for large-scale applications in microelectronics and sensing. To realize this potential, reliable methods for fabricating large-area single-crystalline graphene domains are required. Epitaxial growth on 6H- and 4H-SiC is pursued actively, but achieving large graphene domains with uniform thickness remains a challenge[8]. Graphene synthesis by epitaxy on transition metals has been considered recently[9–14]. Observations of the structural coherence of graphene across steps suggest that the sizes of graphene domains will not be limited by the substrate step spacing in this case[10]. Yet, it remains uncertain if the surface diffusion of carbon adatoms can be of sufficiently long range to achieve sparse graphene nucleation and hence epitaxial graphene domains of macroscopic size. In addition, strong bonding to the support[11] could substantially alter the electronic structure of metal-supported graphene, as well as complicate the separation of graphene sheets from a transition-metal template for transfer to other substrates.

Here, we combine real-time observations of graphene growth by *in situ* surface microscopy with characterization by electron scattering and microscopy, micro-Raman spectroscopy and transport measurements to explore the properties of epitaxial graphene on the (0001) surface of ruthenium (Ru). At high temperatures, a very sparse graphene nucleation enables the growth of truly macroscopic single-crystalline domains with linear dimensions exceeding 200 μm. The ability to nucleate and grow further graphene layers in a controlled way enables determination of the effects of a progressive weakening of substrate interactions on the electronic properties of the epitaxial graphene. Whereas the first graphene layer couples strongly to the Ru substrate, the second layer is essentially decoupled and largely recovers the electronic structure of free-standing graphene. Our findings suggest that single- and few-layer graphene epitaxy on Ru(0001)—and possibly on other transition-metal substrates—integrated by selective growth on transition-metal template pads or combined with methods for transfer to other substrates can provide high-quality material for applications in electronics and sensing.

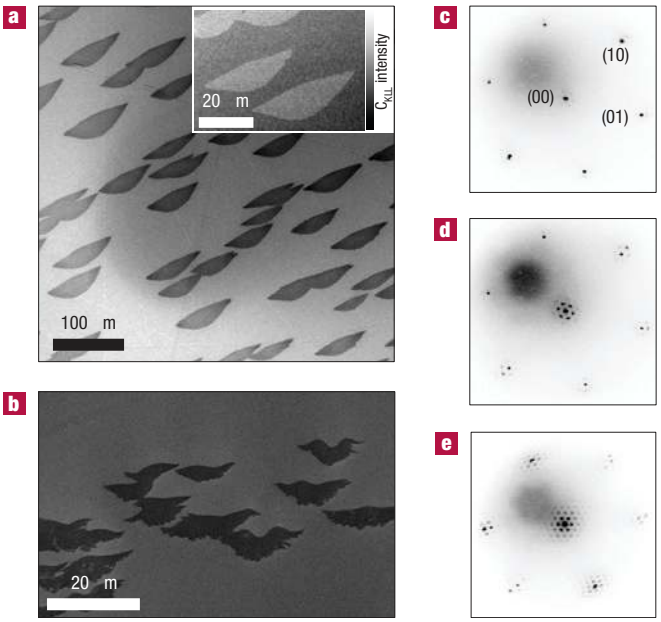

Figure 1 Morphology of epitaxial graphene on Ru(0001). a, UHV-SEM image of a large area of the Ru(0001) surface after first-layer graphene growth. Inset: Carbon KLL (260.6 eV) UHV scanning Auger microscopy image, obtained on this sample. **b**, UHV-SEM image of a group of second-layer graphene islands. **c**, Selected-area low-energy electron diffraction (electron energy: 45.4 eV) pattern of the Ru(0001) substrate. **d**, Diffraction pattern of one-layer epitaxial graphene on Ru(0001) (52.2 eV). **e**, Diffraction pattern of two-layer epitaxial graphene (39.1 eV).

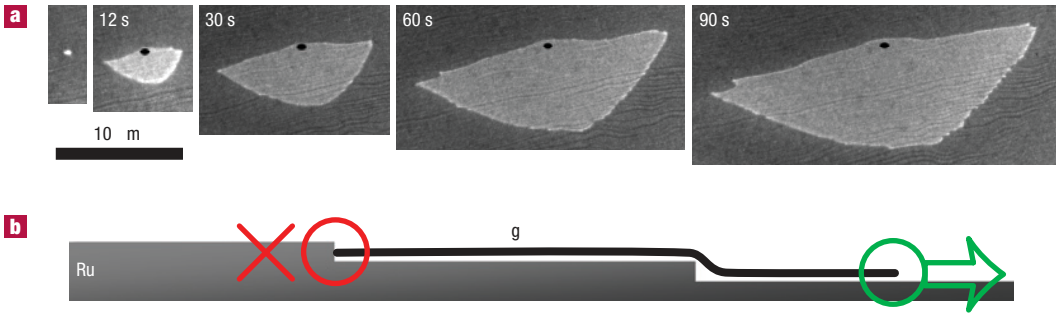

Figure 2 ***In situ*** **microscopy of graphene epitaxy on Ru(0001). a**, Time-lapse sequence of LEEM images showing the initial growth of a first-layer graphene island on Ru(0001) at 850 °C. Numbers indicate elapsed time in seconds after the nucleation of the graphene island. Substrate steps, visible as faint dark lines, are aligned from lower left to upper right. Black dots mark the position of the initial graphene nucleus, demonstrating negligible growth across steps in the 'uphill' direction. **b**, Schematic cross-sectional view of the preferential, carpet-like expansion of the graphene sheet (g) across 'downhill' steps, and suppression of the growth in the 'uphill' direction.

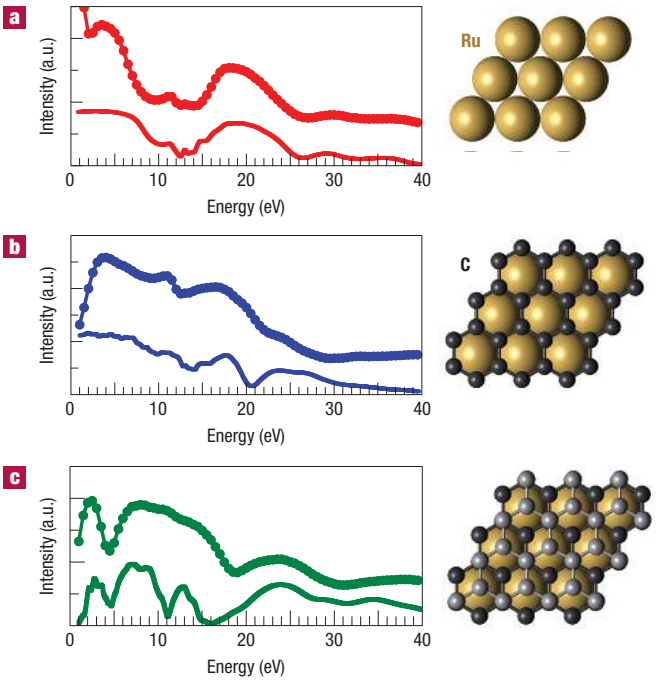

Figure 3 Identification of the layer spacing of one- and two-layer graphene/Ru(0001). a, Measured (top) and simulated (bottom) low-energy electron reflectivity, $I(V)$, of the Ru(0001) substrate. **b**,**c**, Best fit of measured and simulated $I(V)$ spectra for one- and two-layer epitaxial graphene on Ru(0001). Plan-view models of the simulated structures are shown next to the spectra.

We made use of the temperature-dependent solubility of interstitial carbon in transition metals to achieve the controlled layer-by-layer growth of large graphene domains on Ru(0001). At high temperature, C is absorbed into the Ru bulk. Slow cooling from 1,150 °C to 825 °C lowers the interstitial C solubility by a factor of 6 (ref. 15), driving significant amounts of C to the surface. The result is an array of lens-shaped islands of macroscopic size (>100 μm) covering the entire Ru(0001) substrate (Fig. 1a). Ultrahigh-vacuum (UHV) C_{KLL} scanning Auger microscopy shows that these islands are indeed C-rich, and surrounded by Ru metal with negligible C_{KLL} signal. Combining *in situ* electron microscopy and selected-area electron diffraction (Fig. 1c–e), we identify these islands as single-layer epitaxial graphene. On Ru(0001), single-layer graphene adopts an incommensurate moiré structure[11], similar to that observed on other transition metals, such as Ir(111) (ref. 9). Diffraction shows that the $\langle 10\bar{1}0 \rangle$ directions of layer and substrate align, with moiré repeat vectors $a_m = (2.93 \pm 0.08)$ nm, equivalent to 10.8 ± 0.3 times the nearest-neighbour distance on Ru(0001). A marked lowering of the work function compared with that of both clean Ru and bulk graphite indicates strong substrate bonding and significant charge transfer from the metal to the graphene overlayer.

The interaction of the growing islands with atomic substrate steps is an important factor in enabling monocrystalline graphene domains with size exceeding the average step spacing by several orders of magnitude. In contrast to previous work that showed dense nucleation at Ru step edges[11], epitaxial graphene sheets on Ru(0001) nucleate very sparsely and rapidly expand by C incorporation into graphene edge sites under our growth conditions. *In situ* low-energy electron microscopy (LEEM) during growth (Fig. 2) shows a fast expansion of growing graphene domains parallel to substrate steps and across steps in the 'downhill' direction. The crossing of 'uphill' steps by the graphene edge is almost entirely suppressed, leading to a straight boundary that shows virtually no growth. Single-layer graphene should interact with a flat metal substrate primarily through hybridization of the out-of-plane π orbitals with metal d bands, whereas in-plane σ states participate in sp^2 bonding. This picture breaks down when the graphene edge meets a substrate step. The epitaxial orientation on Ru(0001) implies that a graphene sheet projects a zigzag edge with localized dangling σ bonds[16] onto atomic substrate steps. A graphene boundary encountering an 'uphill' step maximizes the orbital overlap and becomes immobilized at the step edge. Conversely, a graphene sheet growing in the 'downhill' direction shows minimal overlap of the edge states with the Ru step, and can flow uninhibited in a carpet-like fashion across the step[10]. This growth mode results in macroscopic graphene domains reaching well over 100 μm in length (Fig. 1a), far larger than the substrate step spacing (0.15 μm), exceeding the extension of the largest monocrystalline epitaxial graphene domains reported so far—below 1 μm on 4H-SiC(000$\bar{1}$) (ref. 17); about 1 μm on Ru(0001) (ref. 12) and Ir(111) (ref. 10)—by at least two orders of magnitude.

If sufficient C segregates from the Ru bulk (or is deposited from a suitable hydrocarbon precursor, such as ethylene[18]), the graphene islands grow to a size corresponding to the spacing of the initial nuclei (>200 μm) and coalesce to a complete first layer[14].

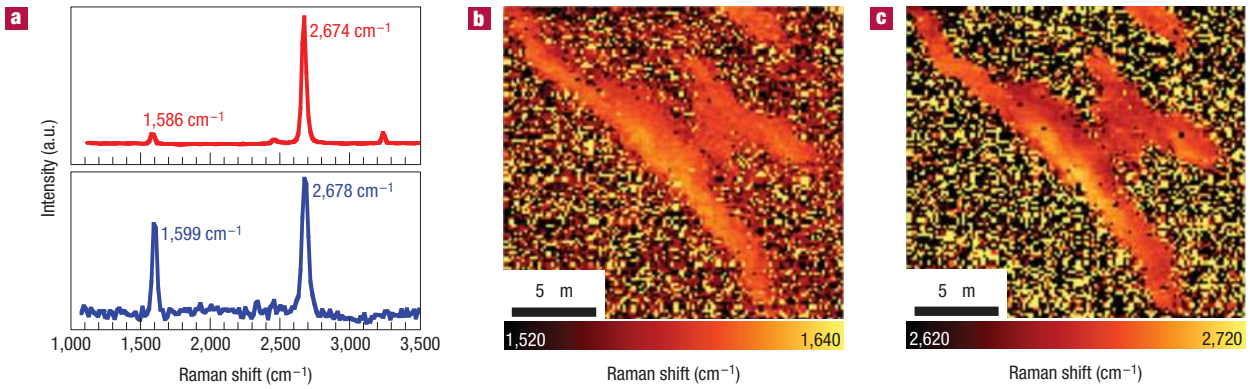

Figure 4 Micro-Raman characterization of two-layer graphene on Ru(0001). a, Comparison of Raman spectra at 532 nm for mechanically cleaved monolayer graphene on SiO_2 (top) and epitaxial two-layer graphene on Ru(0001) (bottom). **b**, Raman map showing the peak energy of the G band for two adjacent two-layer epitaxial graphene islands. **c**, Raman map of the peak energy of the 2D band for the same islands.

At about 80% surface coverage, the nucleation and growth of islands of a second graphene layer are observed (Fig. 1b) on the macroscopic first-layer domains. A smaller separation of second-layer nuclei suggests a C adatom mobility that is lower than on Ru(0001). A well-ordered moiré structure is observed by selected-area diffraction on the second layer (Fig. 1e). Island edges aligned with the direction of substrate steps indicate a residual interaction between Ru(0001) surface steps and graphene edges, similar to that observed for the first layer.

At this point, the surface consists of two different phases. Areas with two-layer graphene coexist with regions covered by a single graphene layer. We expect the first layer to be covalently bonded to the Ru substrate by hybridization of C $2p_z$ orbitals with Ru d-states near the Fermi energy. Charge transfer from the substrate to subsequent graphene layers should diminish progressively, with the interlayer coupling asymptotically approaching the van der Waals interaction of bulk graphite. Assessing this transition is of central importance for evaluating epitaxy on transition metals as a scalable synthesis route of one- or few-layer material with the unique electronic properties of graphene. Going beyond the existing surface-science studies on epitaxial graphene on Ru(0001) (refs 10–14), we have used a combination of structural, vibrational and electronic probes on individual single- and two-layer domains to address this key issue.

The layer spacing has been determined by intensity–voltage LEEM[19], a technique capable of structural fingerprinting in submicrometre surface areas. Spectroscopic stacks of images of a surface were acquired from the (00) diffraction beam as a function of electron energy, V, so that the local image intensity, $I(V)$, represents the specular low-energy electron reflectivity of a given surface domain. When combined with dynamical multiple scattering calculations of the low-energy electron reflectivity[20], this information can be used to determine the spacings of our graphene layer stacks (Fig. 3). We have applied this method to bare Ru(0001), as well as single- and two-layer epitaxial graphene on Ru(0001). Measured and simulated $I(V)$ curves are in excellent agreement for the metal surface (Fig. 3a). On graphene, a best fit between experimental and theoretical $I(V)$ curves is obtained for a unique set of layer spacings. We determine a separation of (1.45 ± 0.1) Å between the Ru substrate and the first graphene layer (Fig. 3b), and a larger spacing of (3.0 ± 0.1) Å between the first and second graphene layer in Bernal (A–B) stacking (Fig. 3c). The addition of the second layer has negligible influence on the separation between the first graphene layer and the metal, which remains fixed at 1.45 Å. This close spacing clearly reflects the strong bonding interaction between Ru and the first graphene layer. Already with the second layer, however, the interlayer spacing comes close to that of bulk graphite (3.34 Å), suggesting that the electronic structure of this and further graphene layers may be affected little by the adjacent metal substrate.

We have used Raman spectroscopy to probe the consequences of this gradual decoupling on the vibrational and electronic properties of transition-metal-supported graphene stacks. Raman spectra on cleaved monolayer and few-layer graphene on SiO_2, which served as reference samples, show two primary features: a G band at ~1,580 cm^{-1} due to the two-fold degenerate E_{2g} mode at the zone centre, and a second-order D* (2D) band at ~2,700 cm^{-1} due to phonons in the highest optical branch near the **K** point at the Brillouin zone boundary[21] (Fig. 4a). The 2D band results from a double-resonance process, which links the phonon wave vectors to the electronic band structure, that is, its line shape can serve as a fingerprint of the electronic structure of massless Dirac fermions of monolayer or few-layer graphene[21].

Figure 4 summarizes micro-Raman experiments at 532 nm excitation on single- and two-layer epitaxial graphene on Ru(0001). The dominant band of the Ru substrate is the transverse-optical zone-centre phonon mode at ~190 cm^{-1} (ref. 22). Samples with a single epitaxial graphene layer show no detectable Raman intensity between 1,000 and 3,000 cm^{-1}. With the addition of the second graphene layer, peaks appear at frequencies close to those of the G and 2D bands (Fig. 4a). Both bands give rise to narrow single peaks, which are shifted to higher energy by 13 cm^{-1} and 4 cm^{-1}, respectively, compared with the same bands in mechanically cleaved monolayer graphene. In Raman maps, the centre position and width of these bands remain constant over large areas within two-layer epitaxial graphene domains several square micrometres in size (Fig. 4b,c). A local blueshift by ~10 cm^{-1} is detected in a continuous area within one of the sampled islands.

The double-resonance process that gives rise to the 2D band has been used to distinguish monolayer and two-layer graphene[21]. For cleaved graphene, the 2D band is defined largely by the dispersion and splitting of electronic bands at the Brillouin zone boundary: a single peak is observed for monolayer graphene, whereas interlayer coupling splits the band into four distinct components for bilayer graphene. The 2D band of two-layer epitaxial graphene on Ru(0001) shows a single peak that is broadened (full-width at half-maximum 42 cm^{-1}) with respect to that of monolayer graphene on SiO_2 (full-width at half-maximum

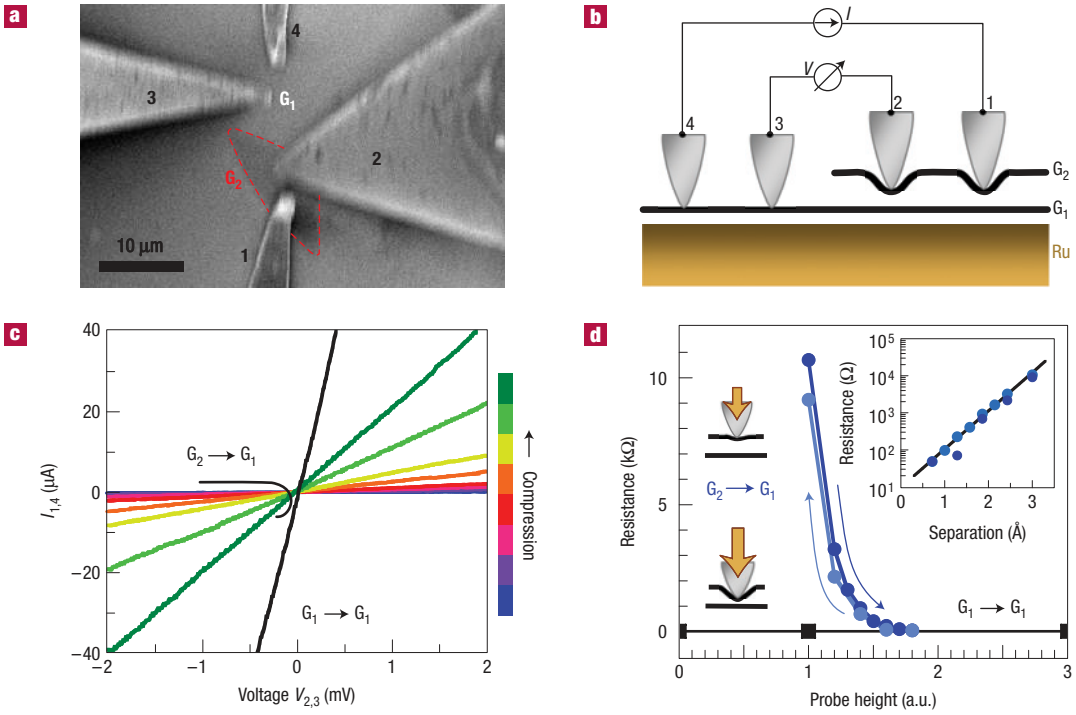

Figure 5 Measurement of interlayer electrical transport. a, UHV-SEM image of the arrangement of four contact probes for interlayer resistance measurement. **b**, Schematic diagram of the four-probe transport measurement between first- and second-layer epitaxial graphene ($G_2 \rightarrow G_1$), using probes 1 and 2 for local mechanical deformation of G_2. **c**, Four-probe current–voltage characteristics for $G_1 \rightarrow G_1$ transport, and for $G_2 \rightarrow G_1$ transport at different compression of the interlayer spacing. **d**, Comparison of the strain dependence of the electrical resistance in $G_1 \rightarrow G_1$ (black squares) and $G_2 \rightarrow G_1$ (blue circles) transport. Dark and light blue curves correspond to mechanical loading and unloading, respectively. Inset: Exponential scaling of interlayer resistance with calculated layer spacing.

38 cm^{-1}). The observation of a single narrow peak suggests that our two-layer samples closely match the electronic structure of cleaved monolayer graphene, with very little observable band splitting due to interaction of the second layer with the underlying graphene layer and Ru metal. Hence, the controlled addition of further epitaxial graphene layers could be used to realize the properties of bilayer and few-layer graphene.

The frequencies and intensity ratios of the G and 2D peaks observed for two-layer graphene on Ru(0001) (Fig. 4a) are consistent with results obtained on cleaved graphene, the carrier density of which is increased by a gate-induced electric field[23–25], suggesting that the Fermi level in the epitaxial two-layer graphene is shifted away from the Dirac point. Chemical doping—reflecting a residual interaction with the underlying metal, indicated by the spacing of the first and second graphene layers and varying slightly across the graphene sheets (Fig. 4b,c)—is the most likely cause.

Both the structural data from intensity–voltage LEEM and the coupled vibrational and electronic signatures in Raman spectroscopy indicate that the second-layer epitaxial graphene on Ru(0001) is strongly decoupled from the metal substrate. This decoupling should also be reflected in the interlayer electronic transport. To evaluate carrier transport through epitaxial graphene stacks, we have carried out room-temperature four-probe transport measurements in UHV, using an instrument that enables the controlled positioning of probes on the sample surface under a field-emission scanning electron microscope (Fig. 5a). Measurements were carried out for two different probe configurations: $G_2 \rightarrow G_1$, two probes each on the first and second graphene layer for measuring transport between graphene sheets; and $G_1 \rightarrow G_1$, all four probes on the first graphene layer.

At identical probe spacing, the measured intralayer and interlayer resistances differ significantly. For voltage probes (2,3) separated by about 10 µm (Fig. 5a), transport in the first graphene layer ($G_1 \rightarrow G_1$) shows a resistance of (10 ± 1) Ω. The interlayer resistance ($G_2 \rightarrow G_1$) is higher by about a factor of 10^3, that is, the electronic coupling between the graphene layers—and hence between the second graphene sheet and the Ru substrate—is weak.

The electronic interaction between sheets with exposed π orbitals is important in a variety of contexts. It determines the anisotropy between the in-plane and *c*-axis conductance of bulk graphite[26], affects electronic transport in multiwall carbon nanotubes[27,28] and nanotube bundles[29] and governs charge transfer in junctions containing π-conjugated molecules[30]. Depending on the alignment of adjacent layers, the interlayer transport involves either hopping or tunnelling between adjacent π orbitals. The coupling mechanism can, in principle, be identified by measuring the interlayer resistance as a function of layer spacing. Early experiments on graphite subjected to high hydrostatic pressures indeed showed a lowering of the *c*-axis resistance at high pressure[31]. A similar type of measurement can be realized on individual micrometre-sized graphene domains using our nanomanipulated electrical probes (Fig. 5b–d). With probes 3 and 4 placed on G_1, probes 1 and 2—in contact with G_2—are moved along the sample normal to deform G_2. The relative stiffness of the tungsten probe tip and the graphene layer generates a large mechanical advantage, *n*, in the range 10^2–10^3, that is, a sub-angstrom deformation of G_2 can be induced controllably by an *n*-fold larger displacement of the tip actuator. Measurements during loading and subsequent unloading coincide exactly, demonstrating that the graphene sheet is strained elastically in this process. Reference measurements with all four

probes placed on G_1 showed no change in electrical characteristics over a much larger range of loading.

Figure 5c,d shows the four-probe resistance as a function of the spacing between G_2 and G_1. For low bias voltages (few millivolts), all measured current–voltage characteristics, $I_{1,4}(V_{2,3})$, are linear. The interlayer resistance varies exponentially with the deformation of G_2, from which we identify direct tunnelling between π-orbitals on the adjacent graphene sheets as the conduction mechanism. We fit the measured resistance to a one-dimensional tunnelling model[30], $I \propto V\exp(-2d\sqrt{2m_e\phi}/\hbar)$, where d and ϕ are the width and constant height (at low V) of the tunnelling barrier, respectively, and m_e denotes the electron (effective) mass. Assuming $m_e = m_0$, we find a barrier height of 5.0 eV, consistent with very weak electronic interlayer coupling of the undeformed graphene stack at room temperature.

Our experiments on a specific model system—single- and two-layer graphene grown epitaxially on a Ru(0001) template—provide evidence for the feasibility of synthesizing large monocrystalline epitaxial graphene domains. A comparison with graphene on SiC, the epitaxial system that has received most attention so far, shows surprisingly similar substrate interactions in both cases: a first graphene layer is spaced closely (1.45 Å for Ru; 1.65 Å for 4H-SiC(000$\bar{1}$) (ref. 32)) and interacts strongly with the substrate, as reflected by a drastic suppression of the work function[33]. This layer, which will have distinct electronic and chemical properties that are yet to be explored, may be seen as a buffer layer supporting the second graphene sheet that is largely decoupled structurally and electronically, but is doped owing to residual charge transfer from the substrate[8]. Significant differences between graphene epitaxy on Ru(0001) and SiC clearly lie in the process conditions and in the level of structural control achievable. Si sublimation on SiC at high temperatures (between 1,250 and 1,450 °C) apparently leads to small (<1 μm) multilayer graphene nuclei. Epitaxy on Ru(0001) at lower temperatures (~850 °C) produces sparse arrays of graphene nuclei that grow in a controlled layer-by-layer mode to macroscopic dimensions.

Our findings open up a number of avenues for exploiting graphene epitaxy on transition-metal templates. The large first-layer graphene domains could be isolated if etch processes are found that selectively remove the Ru substrate but do not damage the graphene layer[1]. It can be predicted that the weakly bound second graphene layer be transferred to another substrate, for example, using intercalation to further weaken the interlayer bonding[34], analogous to the layer transfer methods used successfully for other electronic materials, such as Ge and strained Si (ref. 35). A perhaps more intriguing possibility is the integration with other materials by using lithographically patterned transition-metal pads as a catalyst and template for directed local graphene growth. A similar seeding approach using catalytic Au nanoparticles has been established recently to assemble highly ordered few-layer graphene sheets conformally on semiconductor (Ge (ref. 36), GaN (ref. 37)) nanowires. Finally, our demonstration of an atomic-layer switch, the out-of-plane conductance of which is reversibly altered over three orders of magnitude by tuning the graphene-substrate coupling, suggests the possibility of controlling the in-plane carrier transport in epitaxial or cleaved bilayer or few-layer graphene by 'mechanical gating', that is, local mechanical deformations of the layer stack.

METHODS

GRAPHENE GROWTH AND STRUCTURAL ANALYSIS

Graphene growth was carried out by thermal cycling of a Ru(0001) single crystal in UHV, as described in the text, while observing the process by *in situ* LEEM. Time-lapse LEEM movies were obtained during growth of the first and second epitaxial graphene layer. Selected-area low-energy electron diffraction was carried out on micrometre-sized areas of the bare Ru substrate, as well as the first and second graphene layer. Local intensity–voltage ($I(V)$) characteristics were obtained from real-space images of uniform Ru metal, one-layer and two-layer graphene, acquired as a function of incident electron energy. Layer spacings were determined by comparing measured $I(V)$ characteristics for the specular diffracted beam at very low electron energies (1–40 eV) with simulations by dynamical multiple-scattering low-energy electron diffraction theory[20]. As an approximation to the incommensurate moiré structure observed experimentally, the simulations assumed graphene fully strained to the Ru substrate, with C atoms occupying hexagonal close-packed and face-centred-cubic hollow sites. We thus achieved a faithful representation of the out-of-plane layer separations at reasonable computational efficiency.

MICRO-RAMAN SPECTROSCOPY AND MICROSCOPY

Micro-Raman spectra and Raman maps were obtained on both epitaxial graphene on Ru(0001) and on a reference sample of mechanically cleaved monolayer graphene in a commercial confocal Raman microscope (WiTec). We used an excitation wavelength of 532 nm at incident power below 1 mW, and a ×100 objective providing a diffraction-limited spot size of about 400 nm. Raman maps were acquired by measuring complete spectra on a 0.5 μm grid over a 25 μm × 25 μm sample area. Figure 4b,c was obtained by lorentzian fits to the G and 2D Raman bands, and plotting the spatial distribution of the Raman shifts of these bands.

TRANSPORT MEASUREMENTS

Electrical transport measurements were carried out in UHV in a commercial system (Omicron Nanotechnology) that enables positioning of four independent probe tips with nanometre accuracy on the sample while observing the process by field-emission scanning electron microscopy (SEM). The probes consisted of electrochemically sharpened tungsten wires mounted on and manipulated by piezoelectric actuator elements, and projecting under 45° onto the sample surface. Their tips were placed above selected epitaxial graphene structures, biased relative to the sample, and then approached individually until a tunnelling current was detected. From this tunnelling contact, the tips were carefully brought into mechanical contact, as judged from the onset of linear low-bias four-probe current–voltage characteristics. A controlled compression of the graphene layer G_2 and measurement of the resulting change in interlayer electrical resistance was achieved by driving one of the probes on G_2 closer to the sample using a piezoelectric actuator while measuring both the displacement of the actuator and the four-probe resistance between G_1 and G_2. The different stiffnesses of the probe wire (10 mm long, 0.25 mm diameter) and of the graphene sheet G_2 converted large (several hundred ångströms) movements of the actuator into much smaller deformations of G_2. The resulting reduction of the separation between G_1 and G_2 (Fig. 5d, inset) was inferred from three measured quantities: (1) the relaxed interlayer spacing, $d_0(G_1, G_2) = 3.0$ Å, determined by electron diffraction; (2) the interlayer resistance between the undeformed graphene layer G_2 and the underlying layer G_1 (10 kΩ at $d_0(G_1, G_2) = 3.0$ Å); and (3) the resistance for $G_1 \rightarrow G_1$ transport, assumed equal to the resistance between G_1 and G_2 at zero spacing (10 Ω at $d(G_1, G_2) = 0$). Using the interlayer resistances at 3.0 Å and zero spacing as known end points, an exponential fit to the measured resistance as a function of actuator position provided the conversion between actuator elongation and deformation of G_2, assuming that the two are proportional to each other (that is, differ by a constant factor). All four-probe current–voltage curves were measured with the sample held at room temperature, using a programmable semiconductor test system (Keithley, model 4200SCS).

Received 16 November 2007; accepted 12 March 2008; published 6 April 2008.

References

1. Geim, A. K. & Novoselov, K. S. The rise of graphene. *Nature Mater.* **6**, 183–191 (2007).
2. Novoselov, K. S. *et al.* Two-dimensional gas of massless Dirac fermions in graphene. *Nature* **438**, 197–200 (2005).
3. Bostwick, A. *et al.* Quasiparticle dynamics in graphene. *Nature Phys.* **3**, 36–40 (2007).
4. Novoselov, K. S. *et al.* Electric field effect in atomically thin carbon films. *Science* **306**, 666–669 (2004).
5. Berger, C. *et al.* Electronic confinement and coherence in patterned epitaxial graphene. *Science* **312**, 1191–1196 (2006).
6. Chen, Z., Lin, Y.-M., Rooks, M. J. & Avouris, P. Graphene nano-ribbon electronics. *Physica E* **40**, 228–232 (2007).
7. Schedin, F. *et al.* Detection of individual gas molecules adsorbed on graphene. *Nature Mater.* **6**, 652–655 (2007).
8. de Heer, W. A. *et al.* Epitaxial graphene. *Solid State Commun.* **143**, 92–100 (2007).
9. N'Diaye, A. T., Bleikamp, S., Feibelman, P. J. & Michely, T. Two-dimensional Ir cluster lattice on a graphene moire on Ir(111). *Phys. Rev. Lett.* **97**, 215501 (2006).

10. Coraux, J., N'Diaye, A. T., Busse, C. & Michely, T. Structural coherency of graphene on Ir(111). *Nano Lett.* **8**, 565–570 (2008).
11. Marchini, S., Gunther, S. & Wintterlin, J. Scanning tunneling microscopy of graphene on Ru(0001). *Phys. Rev. B* **76**, 075429 (2007).
12. Vazquez de Parga, A. L. *et al.* Periodically rippled graphene: Growth and spatially resolved electronic structure. *Phys. Rev. Lett.* **100**, 056807 (2008).
13. Pan, Y., Shi, D.-X. & Gao, H.-J. Formation of graphene on Ru(0001) surface. *Chinese Phys.* 3151 (2007).
14. Pan, Y. *et al.* Millimeter-scale, highly ordered single crystalline graphene grown on Ru (0001) surface. Preprint at <http://arxiv.org/abs/0709.2858> (2007).
15. Arnoult, W. J. & McLellan, R. B. The solubility of carbon in rhodium, ruthenium, iridium, and rhenium. *Scr. Metall.* **6**, 1013–1018 (1972).
16. Nakada, K., Fujita, M., Dresselhaus, G. & Dresselhaus, M. S. Edge state in graphene ribbons: Nanometer size effect and edge shape dependence. *Phys. Rev. B* **54**, 17954 (1996).
17. Hass, J. *et al.* Highly ordered graphene for two dimensional electronics. *Appl. Phys. Lett.* **89**, 143106 (2006).
18. Land, T. A. *et al.* STM investigation of single layer graphite structures produced on Pt(111) by hydrocarbon decomposition. *Surf. Sci.* **264**, 261–270 (1992).
19. Schmid, A. K. *et al.* The chemistry of reaction-diffusion fronts investigated by microscopic LEED *I*–*V* fingerprinting. *Surf. Sci. Part 1* **331–333**, 225–230 (1995).
20. Blum, V. & Heinz, K. Fast LEED intensity calculations for surface crystallography using tensor LEED. *Comput. Phys. Commun.* **134**, 392–425 (2001).
21. Ferrari, A. C. *et al.* Raman spectrum of graphene and graphene layers. *Phys. Rev. Lett.* **97**, 187401–187404 (2006).
22. Olijnyk, H., Jephcoat, A. P. & Refson, K. On optical phonons and elasticity in the hcp transition metals Fe, Ru and Re at high pressure. *Europhys. Lett.* **53**, 504–510 (2001).
23. Yan, J., Zhang, Y., Kim, P. & Pinczuk, A. Electric field effect tuning of electron–phonon coupling in graphene. *Phys. Rev. Lett.* **98**, 166802–166804 (2007).
24. Pisana, S. *et al.* Breakdown of the adiabatic Born–Oppenheimer approximation in graphene. *Nature Mater.* **6**, 198–201 (2007).
25. Das, A. *et al.* Electrochemically top gated graphene: Monitoring dopants by Raman scattering. Preprint at <http://arxiv.org/abs/0709.1174> (2007).
26. Matsubara, K., Sugihara, K. & Tsuzuku, T. Electrical resistance in the c direction of graphite. *Phys. Rev. B* **41**, 969 (1990).
27. Bachtold, A. *et al.* Aharonov–Bohm oscillations in carbon nanotubes. *Nature* **397**, 673–675 (1999).
28. Bourlon, B. *et al.* Determination of the intershell conductance in multiwalled carbon nanotubes. *Phys. Rev. Lett.* **93**, 176806 (2004).
29. Bockrath, M. *et al.* Single-electron transport in ropes of carbon nanotubes. *Science* **275**, 1922–1925 (1997).
30. Beebe, J. M. *et al.* Transition from direct tunneling to field emission in metal–molecule–metal junctions. *Phys. Rev. Lett.* **97**, 026801–026804 (2006).
31. Drickamer, H. G. Pi electron systems at high pressure. *Science* **156**, 1712 (1967).
32. Varchon, F. *et al.* Electronic structure of epitaxial graphene layers on SiC: Effect of the substrate. *Phys. Rev. Lett.* **99**, 126805 (2007).
33. Mattausch, A. & Pankratov, O. Ab initio study of graphene on SiC. *Phys. Rev. Lett.* **99**, 076802–076804 (2007).
34. Dresselhaus, M. S. & Dresselhaus, G. Intercalation compounds of graphite. *Adv. Phys.* **51**, 1–186 (2002).
35. Maleville, C. & Mazure, C. Smart-cut technology: From 300 mm ultrathin SOI production to advanced engineered substrates. *Solid State Electron.* **48**, 1055–1063 (2004).
36. Sutter, P. W. & Sutter, E. A. Dispensing and surface-induced crystallization of zeptolitre liquid metal-alloy drops. *Nature Mater.* **6**, 363–366 (2007).
37. Sutter, E. *et al.* Assembly of ordered carbon shells on GaN nanowires. *Appl. Phys. Lett.* **90**, 093118 (2007).

Acknowledgements

The authors thank T. Valla and J. Camacho for access to a cleaved monolayer graphene sample. Work carried out under the auspices of the US Department of Energy under contract No. DE-AC02-98CH1-886.

Author contributions

P.W.S. and E.A.S. planned the study, carried out all experiments, and analysed the data. J.-I.F. carried out the LEED $I(V)$ simulations. P.W.S. wrote the paper, and all authors commented on the manuscript.

Author information

Reprints and permission information is available online at http://npg.nature.com/reprintsandpermissions. Correspondence and requests for materials should be addressed to P.W.S.